

Nonsymmorphic symmetry protected node-line semimetal in the trigonal YH_3

Dexi Shao¹, Tong Chen¹, Qinyan Gu¹, Zhaopeng Guo¹, Pengchao Lu¹, Jian Sun^{1*}, Li Sheng¹, and Dingyu Xing¹

¹National Laboratory of Solid State Microstructures, School of Physics and Collaborative Innovation Center of Advanced Microstructures, Nanjing University, Nanjing 210093, China

*jjiansun@nju.edu.cn

ABSTRACT

Using ab initio calculations based on density-functional theory and effective model analysis, we propose that the trigonal YH_3 (Space Group: $\bar{P}3c1$) at ambient pressure is a node-line semimetal when spin-orbit coupling (SOC) is ignored. This trigonal YH_3 has very clean electronic structure near Fermi level and its nodal lines locate very closely to the Fermi energy, which makes it a perfect system for model analysis. Symmetry analysis shows that the nodal ring in this compound is protected by the glide-plane symmetry, where the band inversion of $|Y^+, d_{xz}\rangle$ and $|H1^-, s\rangle$ orbits at Γ point is responsible for the formation of the nodal lines. When SOC is included, the line nodes are prohibited by the glide-plane symmetry, and a small gap (≈ 5 meV) appears, which leads YH_3 to be a strong topological insulator with Z_2 indices (1,000). Thus the glide-plane symmetry plays an opposite role in the formation of the nodal lines in cases without and with SOC. As the SOC-induced gap is so small that can be neglected, this $\bar{P}3c1$ YH_3 may be a good candidate for experimental explorations on the fundamental physics of topological node-line semimetals. We find the surface states of this $\bar{P}3c1$ phase are somehow unique and may be helpful to identify the real ground state of YH_3 in the experiment.

Introduction

Topological semimetals (TSMs) have attracted great attention for both theoretical interests and experimental applications in recent years. Different from time-reversal symmetry (TRS) protected Z_2 topological insulators (TIs)^{1,2} which are insulating in the bulk, TSMs are materials where the conduction and the valence bands cross with each other at certain locations in the Brillouin Zone (BZ). Usually, the band crossing is protected by certain symmetries, i.e., perturbations on the Hamiltonian which respect the symmetries can not break the crossing. Recently, several types of TSMs have been proposed to investigate the fermion-like excitations, including Dirac fermions,³⁻⁶ Weyl fermions⁷⁻¹⁰ and nodal lines.¹¹⁻¹⁶ These compounds are named as: Dirac semimetals (DSMs), Weyl semimetals (WSMs) and node-line semimetals (NLSMs), respectively.

Up to now, there have been a lot of reports about the progress in DSMs and WSMs, for example, 3D Dirac semimetals have recently been identified experimentally in Cd_3As_2 ¹⁷⁻²¹ and Na_3Bi systems.^{22,23} Similarly, TaAs ,^{9,24-26} NbAs ,²⁷ TaP ,²⁸ WTe_2 ,^{29,30} and MoTe_2 ³¹ etc are verified to be WSMs experimentally in recent years. Different from DSMs and WSMs, in which the conduction and valence bands touch at discrete points, the crossings of NLSMs form a closed loop in the BZ. Although many candidates of NLSMs have been proposed and much efforts has been made to investigate them, the corresponding progress in the experiment is slow, because an open surface usually breaks the inversion or some mirror symmetries which are important to the formation of nodal lines.³²

Materials experimentally confirmed (or partially confirmed) to host nodal line include Be metal,¹⁶ ZrSiS ,³³ PbTaSe_2 ¹⁴ and ZrSiSe/ZrSiTe .³⁴ Therefore, theoretical predictions on more candidates of node-line semimetal are still in demand. It is well known that symmetries play important roles in identifying various of TIs and topological superconductors (TSCs).³⁵⁻³⁹ In fact, symmetries are also important in classifying NLSMs, for instance, three types of NLSMs protected by different symmetries have been proposed: (a) mirror symmetry protected NLSMs,^{8,14,16,40} (b) coexistence of TRS and inversion symmetry (IS) protected NLSMs^{11-13,32} and (c) nonsymmorphic symmetry protected NLSMs.^{15,32}

Hydrides is a large class of materials and has been extensively investigated in many aspects, including energy storage⁴¹ and superconductivity,⁴²⁻⁴⁶ etc. Since Ashcroft proposed that high T_c superconductivity can be obtained in hydrogen and hydrides under high pressure,^{47,48} many hydrides have been investigated. Yttrium-hydrogen system becomes interesting due to the same reason. For instance, a fcc YH_3 has been predicted to be a superconductor with $T_c \sim 40$ K at 17.7 GPa.⁴⁹ Later work predicts that two new yttrium hydrides, i.e., YH_4 and YH_6 , are also superconductors with $T_c \sim 84 - 95$ K and $T_c \sim 251 - 264$ K at 120 GPa, respectively.⁵⁰ Very recently, YH_{10} in the space group of both $Im\bar{3}m$ and $Fm\bar{3}m$ has been predicted to be a

Table 1. The experimental lattice parameters of YH₃ with P $\bar{3}$ c1 symmetry.⁷¹

phase	a=b	c	$\alpha = \beta$	γ
P $\bar{3}$ c1	6.359 (Å)	6.607 (Å)	90°	120°

room-temperature superconductor under very high pressure.^{51,52}

Though many works about superconductivity of yttrium-hydrogen system under pressure have been implicated, very few explorations on the topological electronic properties of hydrides have been reported so far.^{53–55} In this work, we predicted that YH₃ in the space group of P $\bar{3}$ c1 at ambient pressure is a node-line semimetal when spin-orbit coupling (SOC) is ignored. Especially, the YH₃ system we studied has extremely clean electronic structures near the Fermi level; i.e., there are no other pockets. The energy of the crossing points along the nodal loop varies within a very small energy range, from around -5 to 35 meV. Therefore, this nodal loop is very "flat" in the energy and momentum space, which makes YH₃ a perfect model system for NLSMs. In general, NLSMs without SOC will transform into either insulators, DSMs, WSMs or even double NLSMs when SOC is considered, which is much related to the symmetries in the corresponding systems.⁵⁶ While in this work, when SOC is included, the three nodal lines around Γ point will be gapped out with a small gap (≈ 5 meV), making YH₃ a topological insulator with $Z_2=(1,000)$. Nevertheless, further calculation shows that the gap induced by SOC along the nodal ring is very small (about 5 meV), which indicates that the effect of SOC is negligible and the characteristic of the nodal ring can be preserved.

Methods

Calculations of the band structures are performed using the full-potential linearized augmented plane-wave (FP-LAPW) method^{57,58} implemented in the WIEN2k⁵⁹ package. We use $13 \times 13 \times 11$ k-mesh for the BZ sampling and -7 for the plane wave cut-off parameter $R_{MT}K_{max}$ for the electronic structure calculation, where the R_{MT} is the minimum muffin-tin radius and K_{max} is the plane-wave vector cut-off parameter. SOC is taken into consideration by a second-variation method.⁶⁰ The tight-binding models are constructed with the maximally localized Wannier functions (MLWFs) method,^{61–63} the corresponding hopping parameters are determined from the projections of the bulk Bloch wave functions. The projected surface states are calculated using surface Green's function in the semi-infinite system.^{64,65}

Results and discussions

The crystal structure of YH₃. Historically, three different phases of YH₃ have been reported to be the ground state potentially. Two of them are experimentally favoured with trigonal P $\bar{3}$ c1 and hexagonal P6₃cm symmetry,^{66–71} while the third candidate is in the space group of P6₃ which was predicted theoretically.⁷² It seems that the ground state of YH₃ at ambient pressure is still under debate because the three candidates have very tiny total energy difference (0.001 eV/f.u.) from theoretical point of view. First, the hexagonal P6₃ structure is only theoretically proposed and seems to disagree with the neutron-diffraction results.^{73,74} Second, later neutron-diffraction experiments^{71,75} identify that the P $\bar{3}$ c1 structure is stable from the ambient pressure up to 12GPa. Thus, in the following, we only focus on the phase of YH₃ with the P $\bar{3}$ c1 symmetry.

The crystal structure and corresponding BZ of P $\bar{3}$ c1 (Space Group No. 165) YH₃ is shown in Fig. 1(a) and Fig. 1(b) respectively. We use the experimental lattice parameters from literature⁷¹ in our calculations, which are listed in Table. 1.

Band structures without SOC and the corresponding model analysis. From the band structures of P $\bar{3}$ c1 YH₃ without SOC shown in Fig. 2(a), we can find three Dirac crossings composed of the conduction band minimum (CBM) and the valence band maximum (VBM) near Γ along the high-symmetry path in the BZ at the first sight. Detailed first-principle calculations indicates that Dirac crossings lying in the plane $m_{\Gamma-M-L-A}$ is protected by the G_x symmetry, while Dirac crossing along $K \rightarrow \Gamma$ is not symmetry-protected (both the irreducible representations of CBM and VBM are Γ_2) i.e., hybridization between the CBM and the VBM will open a gap in-between. Further calculations indicates that the CBM and the VBM are contributed mainly by Y-d_{xz} and H1-s orbits, respectively, as the fat-band showed in Fig. 2(a). The band inversion (not caused by SOC) of Y-d_{xz} and H1-s at Γ point leads to a gap of 0.302 eV.

To give more insights of the nodal lines surrounding the Γ point, we have established an effective Hamiltonian by $\mathbf{k} \cdot \mathbf{p}$ method. Taking the crystal symmetry and TRS into consideration, the effective Hamiltonian can be written as follows:

$$\begin{aligned}
H(\vec{k}) &= g_0(\vec{k})\tau_0 + g_x(\vec{k})\tau_x + g_z(\vec{k})\tau_z \\
g_0(\vec{k}) &= M_0 - B_0(k_x^2 + k_y^2) - C_0k_z^2 \\
g_x(\vec{k}) &= A(k_x^3 - 3k_xk_y^2) \\
g_z(\vec{k}) &= M_z - B_z(k_x^2 + k_y^2) - C_zk_z^2.
\end{aligned} \tag{1}$$

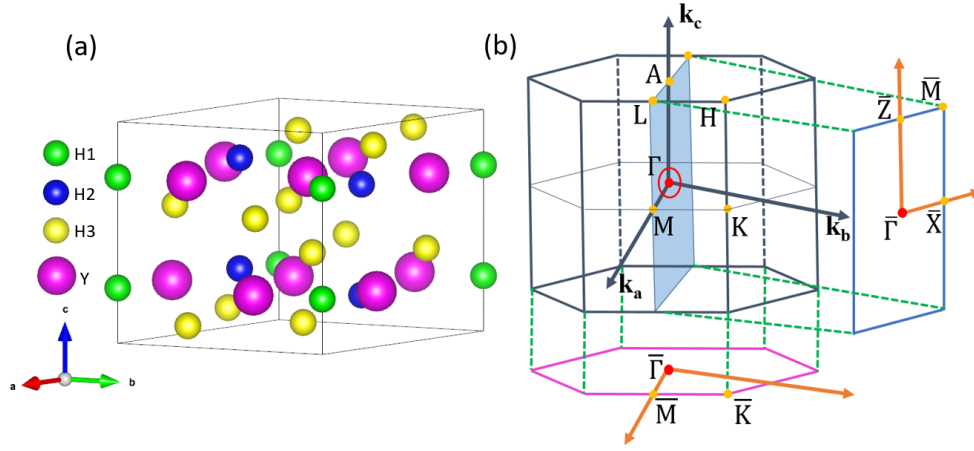


Figure 1. (a) Crystal structure of YH_3 at the ambient pressure with $\text{P}\bar{3}\text{c}1$ symmetry. H1, H2 and H3 atoms occupy the 2a $(0,0,\frac{1}{4})$, 4d $(\frac{1}{3},\frac{2}{3},0.181)$ and 12g $(0.348,0.025,0.093)$ sites, respectively, while Y atoms lie at the 6f $(0.336,0,\frac{1}{4})$ sites. (b) The corresponding BZ and its projection onto the (010) direction. The red ring on the shadow plane surrounding the Γ point represents the node-line structure in the BZ.

Table 2. The character table for the $\text{P}\bar{3}\text{c}1$ YH_3 .

Γ	Representation	T/P	\vec{k}
Γ_1	$\tilde{\Gamma}_1^+ / A_{1g}$	+	$1, k_x^2 + k_y^2, k_z^2$
Γ_2	$\tilde{\Gamma}_2^- / A_{2u}$	-	$k_z, k_z^3, 3k_x^2k_y - k_y^3$
Γ_3	$\tilde{\Gamma}_1^- / A_{1u}$	-	$k_x^3 - 3k_xk_y^2$
$\{\Gamma_4, \Gamma_5\}$	$\tilde{\Gamma}_3^- / E_u$	-	$\{k_x, k_y\}, \{k_x^3 + k_xk_y^2, k_x^2k_y + k_y^3\}$

Here, the τ_x and τ_z are Pauli matrices, τ_0 is a 2×2 unit matrix. This system has both TRS and IS, thus, the component of τ_y must be zero.¹¹ We can obtain the eigenvalues of the two-level system by diagonalizing the 2×2 effective Hamiltonian and the results are $E(\vec{k}) = g_0(\vec{k}) \pm \sqrt{g_x^2 + g_z^2}$. Band crossings of the nodal lines will occur when $g_x = g_z = 0$. It's clear that $g_z(\vec{k}) = 0$ gives us $M_z B_z > 0$ and $M_z C_z > 0$. We find that $M_z B_z > 0$ and $M_z C_z > 0$ are exactly the condition of band inversion. Furthermore, $g_x(\vec{k}) = 0$ confines the band crossings of the node-line in the $k_x = 0, \pm\sqrt{3}k_y$ planes, i.e., there are three nodal rings surrounding the Γ point and lying in mirror-invariant planes $m_{\Gamma-M-L-A}$, as shown with the shadow sector in Fig. 1(b). It's obvious that these three nodal rings are related to each other by R_{3z} symmetry.

Band structures with SOC and the corresponding model analysis. When SOC is considered, band crossings of the three nodal lines will disappear, as the corresponding band structure with SOC shown in Fig. 2(b). We will further explain the above-mentioned phenomenon in the following. Taking SOC into account, spin and orbital angular momentum are coupled together, which generates a group of new eigenstates with certain total angular momentum quantum numbers. Then we can mark these new eigenstates of the CBM and VBM as $|H1_s^-, \pm\frac{1}{2}\rangle$, and $|Y_{d_{xz}}^+, \pm\frac{1}{2}\rangle$. Here subscripts s and d_{xz} denote corresponding orbits consisting of the new eigenstates and the superscripts \pm represent the parities of corresponding eigenstates, respectively.

According to the analysis of irreducible representations and projected orbits, the CBM and VBM at the Γ point (denoted as Γ_4^- and Γ_4^+) are mainly composed of $|H1_s^-, \pm\frac{1}{2}\rangle$ and $|Y_{d_{xz}}^+, \pm\frac{1}{2}\rangle$ basis, respectively. If we arrange the 4 basis in the order of $|H1_s^-, \frac{1}{2}\rangle, |H1_s^-, -\frac{1}{2}\rangle, |Y_{d_{xz}}^+, \frac{1}{2}\rangle, |Y_{d_{xz}}^+, -\frac{1}{2}\rangle$, and then take the time-reversal and D_{3d} point-group symmetries at the Γ point into consideration, we can give the character table of Γ matrices and the polynomials of momentum \vec{k} for this system as shown in Table. 2.

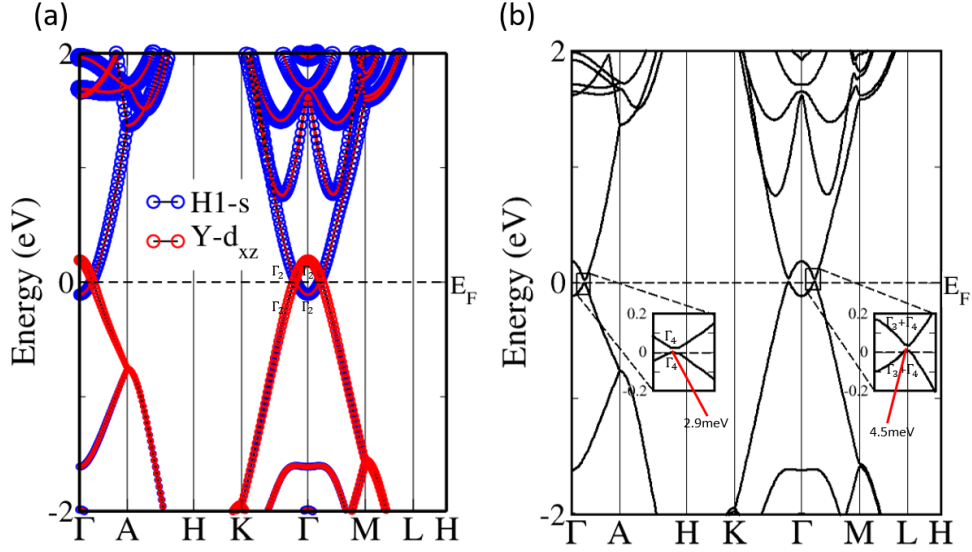


Figure 2. (a) Corresponding fat-band structure of YH₃ in the space group of $P\bar{3}c1$ without SOC. The bands between CBM and VBM is gapped along $K \rightarrow \Gamma$ as the irreducible representations have showed. (b) Corresponding band structure of YH₃ in the space group of $P\bar{3}c1$ with SOC.

From Table. 2, our model Hamiltonian yields as

$$\begin{aligned}
 H(\vec{k}) &= \varepsilon_0(\vec{k}) + \sum_{i=1}^5 f_i(\vec{k}) \Gamma_i \\
 &= \varepsilon_0(\vec{k}) + \begin{pmatrix} M(\vec{k}) & 0 & A(\vec{k}) & C(\vec{k}) \\ 0 & M(\vec{k}) & C^*(\vec{k}) & B(\vec{k}) \\ A^*(\vec{k}) & C(\vec{k}) & -M(\vec{k}) & 0 \\ C^*(\vec{k}) & B^*(\vec{k}) & 0 & -M(\vec{k}) \end{pmatrix}
 \end{aligned} \tag{2}$$

which describes the dispersion of the CBM and VBM around the Γ point. Here we use the following Γ matrices:

$$\begin{aligned}
 \Gamma_1 &= \sigma_3 \otimes \tau_0 & \Gamma_2 &= \sigma_1 \otimes \tau_3 & \Gamma_3 &= \sigma_2 \otimes \tau_0 \\
 \Gamma_4 &= \sigma_1 \otimes \tau_1 & \Gamma_5 &= \sigma_1 \otimes \tau_2,
 \end{aligned} \tag{3}$$

which satisfy the Clifford algebra $\{\Gamma_a, \Gamma_b\} = 2\delta_{ab}$. While the other ten Γ matrices are given by $\Gamma_{ab} = \frac{1}{2i}[\Gamma_a, \Gamma_b]$. Presence of both TRS and IS will forbid the existence of these ten Γ_{ab} terms in our model Hamiltonian. In Equation (2), $\varepsilon_0(\vec{k}) = D_0 - m_0 k_z^2 - n_0(k_x^2 + k_y^2)$, $M(\vec{k}) = D_1 - m_1 k_z^2 - n_1(k_x^2 + k_y^2)$, $A(\vec{k}) = D_2 k_z + E_2 k_z^3 + F_2(3k_x^2 k_y - k_y^3) - iD_3(k_x^3 - 3k_x k_y^2)$, $B(\vec{k}) = -D_2 k_z - E_2 k_z^3 - F_2(3k_x^2 k_y - k_y^3) - iD_3(k_x^3 - 3k_x k_y^2)$ and $C(\vec{k}) = D_{45} k_- + E_{45}(k_x^2 + k_y^2) k_-$ with $k_- = k_x - ik_y$.

From the model Hamiltonian given in Equation. (2) together with the band structure shown in Fig. 1(b), we can draw some conclusions as the following. First of all, $\varepsilon_0(\vec{k})$ will break the particle-hole symmetry for the CBM and VBM around the Γ point. Secondly, D_1 in $M(\vec{k})$ will lead to a gap at the Γ point. Thirdly, to reproduce band inversion, we need that $D_1 m_1 > 0 \cap D_1 n_1 > 0$. More importantly, the dispersions of the model Hamiltonian given by Equation. (2) are $E(\vec{k}) = f_0(\vec{k}) \pm \sqrt{f_1^2(\vec{k}) + f_2^2(\vec{k}) + f_3^2(\vec{k}) + f_4^2(\vec{k}) + f_5^2(\vec{k})}$ and both dispersions are doubly degenerate. As a result, a band crossing of this model requires $f_1 = f_2 = f_3 = f_4 = f_5 = 0$. There are several discrete \vec{k} points near the Γ point may satisfy the above-mentioned conditions. For example, $\vec{k} = (0, 0, \pm \sqrt{-\frac{D_2}{E_2}})$ when $D_2 E_2 < 0 \cap \frac{D_1}{m_1} = -\frac{D_2}{E_2}$ stands. It means that we may find some Dirac crossings at the first sight. However, on one hand, $\frac{D_1}{m_1} = -\frac{D_2}{E_2}$ is a very rigorous condition and can not be obtained without other symmetries. More importantly, on the other hand, we can explain that \vec{k} points lying in the plane $m_{\Gamma-M-L-A}$ must induce a gap in the following. There are three generator operators existing in the nonsymmorphic space group $P\bar{3}c1$, we

Table 3. The parities product of all the occupied bands at the eight TRIMs for the $P\bar{3}c1$ phase of YH_3 .

TRIM	Γ	3M	A	3L ;	total
Parity	+	-	-	- ;	-

sign the three-fold rotation axis around z axis, the glide plane located at $x = 0$, and the inversion symmetry as R_{3z} , G_x and P , respectively. The operation of G_x acts in both the real space (x, y, z) and the spin space as

$$\begin{aligned} G_x : (x, y, z) &\rightarrow (-x, y, z + \frac{1}{2}) \\ G_x : (s_x, s_y, s_z) &\rightarrow (s_x, -s_y, -s_z). \end{aligned} \quad (4)$$

Similar with the analysis in the work by Fang et al.,³² we can easily find

$$G_x * (P * T) = e^{-ik_z} (P * T) * G_x. \quad (5)$$

On the mirror invariant plane $k_x = 0$, the bands can be labeled by its G_x eigenvalues. When SOC is considered, we have

$$G_x^2 = -e^{-ik_z} \quad (6)$$

the minus sign is because G_x^2 includes a 2π rotation in the spin space, which gives a -1 for a spin- $\frac{1}{2}$ system. So the eigenvalue of G_x is $\pm ie^{-i\frac{k_z}{2}}$. The existence of both P and T will preserve all bands locally degenerated at every \vec{k} point in the BZ when SOC is considered, and the degenerated bands are related to each other by $P * T$. Suppose at $(0, k_y, k_z)$, a Bloch function $|\psi(\vec{k})\rangle$ is an eigenstate of G_x with eigenvalue $ie^{-i\frac{k_z}{2}}$, then its degenerate partner $P * T|\psi(\vec{k})\rangle$ under G_x ,

$$\begin{aligned} G_x(P * T)|\psi(\vec{k})\rangle &= e^{-ik_z} (P * T)G_x|\psi(\vec{k})\rangle \\ &= e^{-ik_z} (P * T)ie^{-i\frac{k_z}{2}}|\psi(\vec{k})\rangle \\ &= -ie^{-i\frac{k_z}{2}} (P * T)|\psi(\vec{k})\rangle. \end{aligned} \quad (7)$$

It means that the degenerated bands on the $k_x = 0$ plane have opposite G_x eigenvalues, and two sets of such doublet bands generally anticross, i.e., the bands with the same G_x eigenvalues hybridize and avoid crossing. In other words, nodal lines near the Γ point in the $k_x = 0$ plane (without SOC) will disappear in the whole BZ when SOC is considered, and G_x symmetry plays the key role of prohibiting the band crossing between CBM and VBM, even though the gap is very small (≈ 5 meV) as the $\mathbf{k} \cdot \mathbf{p}$ Hamiltonian in Equation(2) has showed us. As a result, this node-line semimetal will become an insulator when SOC is considered. With both TRS and IS in this system, we can easily calculate the Z_2 index by multiplying all the parities of all the occupied bands at all time-reversal-invariant momenta (TRIMs) using the method by Fu and Kane.⁷⁶ The results are shown in Table. 3, which indicates the $P\bar{3}c1$ YH_3 is a strong TI with $Z_2 = (1, 000)$ when SOC is taken into consideration. Nevertheless, the effect of the SOC is negligible because the H atom is small and the Y atom is also not very heavy; there is only one d electron in the Y atom. We have performed calculations with SOC and found that the SOC induced gap along the nodal ring is very small (about 5 meV), which indicates that the effect of SOC could be ignored and the characteristic of the nodal ring can be preserved.

Surface states with and without SOC. Exotic topological surface states are an important property to identify various topological phases. Based on the tight-binding model constructed with WLWFs and surface Green function methods,^{64,65,77} we have calculated the $\langle 010 \rangle$ surface states of the $P\bar{3}c1$ YH_3 without SOC and the $\langle 001 \rangle$ surface states with SOC, as shown in Fig. 3(a) and Fig. 3(b), respectively. In particular, as the nice picture shows in Fig. 3(a), topological protected surface states without SOC signed with a bright curve connects the nodal points across the boundary of BZ. When SOC is included, the gap along $\Gamma \rightarrow A$ is so small (≈ 5 meV) that we may consider the CBM and VBM are nearly touched in the bulk band structure, this phenomenon can be proved that we can find the corresponding $\langle 001 \rangle$ surface states connecting the pseudo-touch points from Fig. 3(b). We think these topological protected surface states may be helpful to identify the real ground state of YH_3 from those three candidates. For example, we propose that angle-resolved photoemission spectroscopy (ARPES) technique can be used to investigate these surface states of this node-line semimetal candidate. If a bright surface state could be found in the $\langle 010 \rangle$ direction, and two parabolic bright curves with negative mass touching at the $\bar{\Gamma}$ point could be found in the $\langle 001 \rangle$ direction, then the YH_3 sample should be in the $P\bar{3}c1$ symmetry.

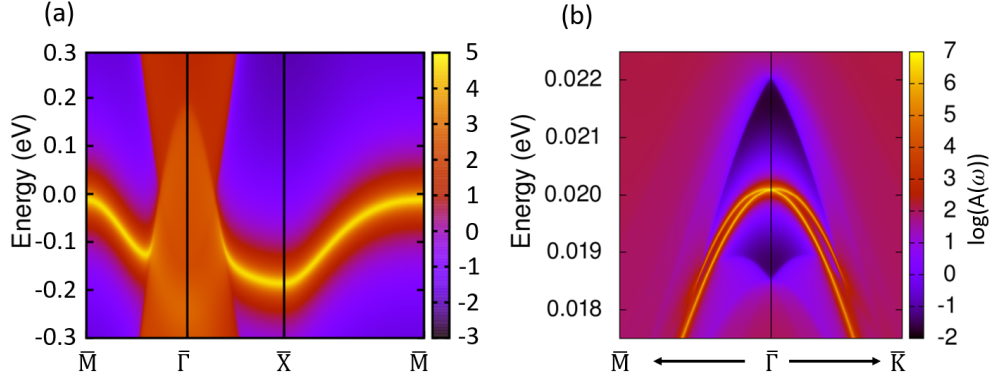


Figure 3. (a)The surface states without SOC of $\bar{P}3c1$ YH_3 terminated with H atoms in the $\langle 010 \rangle$ direction, (b)The surface states with SOC of $\bar{P}3c1$ YH_3 terminated with H atoms in the $\langle 001 \rangle$ direction.

Conculsion

In conclusion, based on first-principles calculations and effective model analysis, we propose that the $\bar{P}3c1$ YH_3 is a nonsym-morphic symmetry protected node-line semimetal when SOC is ignored. This system has very clean electronic structures, there are no other pockets except the ones composing the node line near the Fermi level. The energy of the crossing points along the nodal loop has a very small energy range, from around -5 to 35 meV. Therefore, this nodal loop is very “flat” in the energy and momentum space, which makes YH_3 a perfect system for model analysis. There are three node-lines related to each other by R_{3z} symmetry locating on three planes (signed as $m_{\Gamma-M-L-A}$) surrounding the Γ point. While SOC is taken into consideration, the band crossings consisting of these node-lines will be gapped, and the $\bar{P}3c1$ YH_3 becomes a strong topological insulator with Z_2 indices (1,000). At last, we have calculated the surface states of this system to verify its topological properties. We think our predictions should be helpful to identify the real ground state of YH_3 in experiments in the future.

References

1. Hasan, M. Z. & Kane, C. L. Colloquium : Topological insulators. *Rev. Mod. Phys.* **82**, 3045 (2010).
2. Qi, X.-L. & Zhang, S.-C. Topological insulators and superconductors. *Rev. Mod. Phys.* **83**, 1057 (2011).
3. Wang, Z. *et al.* Dirac semimetal and topological phase transitions in A_3Bi ($A = Na, K, Rb$). *Phys. Rev. B* **85**, 195320 (2012).
4. Wang, Z., Weng, H., Wu, Q., Dai, X. & Fang, Z. Three-dimensional Dirac semimetal and quantum transport in Cd_3As_2 . *Phys. Rev. B* **88**, 125427 (2013).
5. Young, S. M. *et al.* Dirac semimetal in three dimensions. *Phys. Rev. Lett.* **108**, 140405 (2012).
6. Gibson, Q. D. *et al.* Three-dimensional Dirac semimetals: Design principles and predictions of new materials. *Phys. Rev. B* **91**, 205128 (2015).
7. Wan, X., Turner, A. M., Vishwanath, A. & Savrasov, S. Y. Topological semimetal and fermi-arc surface states in the electronic structure of pyrochlore iridates. *Phys. Rev. B* **83**, 205101 (2011).
8. Xu, G., Weng, H., Wang, Z., Dai, X. & Fang, Z. Chern semimetal and the quantized anomalous hall effect in $HgCr_2Se_4$. *Phys. Rev. Lett.* **107**, 186806 (2011).
9. Lv, B. Q. *et al.* Experimental discovery of weyl semimetal TaAs. *Phys. Rev. X* **5**, 031013 (2015).
10. Xu, S. Y. *et al.* TOPOLOGICAL MATTER. Discovery of a Weyl fermion semimetal and topological Fermi arcs. *Science* **349**, 613 (2015).
11. Weng, H. *et al.* Topological node-line semimetal in three-dimensional graphene networks. *Phys. Rev. B* **92**, 045108 (2015).
12. Kim, Y., Wieder, B. J., Kane, C. L. & Rappe, A. M. Dirac Line Nodes in Inversion-Symmetric Crystals. *Phys. Rev. Lett.* **115**, 036806 (2015).
13. Yu, R., Weng, H., Fang, Z., Dai, X. & Hu, X. Topological node-line semimetal and Dirac semimetal state in antiperovskite Cu_3PdN . *Phys. Rev. Lett.* **115**, 036807 (2015).

14. Bian, G. *et al.* Topological nodal-line fermions in spin-orbit metal PbTaSe₂. *Nat. Commun.* **7**, 10556 (2016).
15. Bzdusek, T., Wu, Q., Ruegg, A., Sigrist, M. & Soluyanov, A. A. Nodal-chain metals. *Nature* **538**, 75 (2016).
16. Li, R. *et al.* Dirac Node Lines in Pure Alkali Earth Metals. *Phys. Rev. Lett.* **117**, 096401 (2016).
17. Liu, Z. K. *et al.* A stable three-dimensional topological Dirac semimetal Cd₃As₂. *Nat. Mater.* **13**, 677 (2014).
18. Neupane, M. *et al.* Observation of a three-dimensional topological Dirac semimetal phase in high-mobility Cd₃As₂. *Nat. Commun.* **5**, 3786 (2014).
19. Borisenko, S. *et al.* Experimental realization of a three-dimensional Dirac semimetal. *Phys. Rev. Lett.* **113**, 027603 (2014).
20. Yi, H. *et al.* Evidence of topological surface state in three-dimensional Dirac semimetal Cd₃As₂. *Sci. Rep.* **4**, 6106 (2013).
21. Jeon, S. *et al.* Landau quantization and quasiparticle interference in the three-dimensional Dirac semimetal Cd₃As₂. *Nat. Mater.* **13**, 851 (2014).
22. Chen, Y. L. *et al.* Discovery of a three-dimensional topological Dirac semimetal, Na₃Bi. *Science* **343**, 864 (2014).
23. Xu, S. Y. *et al.* Observation of Fermi arc surface states in a topological metal. *Science* **347**, 294 (2015).
24. Huang, X. *et al.* Observation of the Chiral-Anomaly-Induced Negative Magnetoresistance in 3D Weyl Semimetal TaAs. *Phys. Rev. X* **5**, 031023 (2015).
25. Lv, B. *et al.* Observation of Weyl nodes in TaAs. *Nat. Phys.* **11**, 724 (2015).
26. Lv, B. Q. *et al.* Observation of Fermi-Arc Spin Texture in TaAs. *Phys. Rev. Lett.* **115**, 217601 (2015).
27. Xu, S.-Y. *et al.* Discovery of a Weyl fermion state with Fermi arcs in niobium arsenide. *Nat. Phys.* **11**, 748 (2015).
28. Xu, N. *et al.* Observation of Weyl nodes and Fermi arcs in tantalum phosphide. *Nat. Commun.* **7**, 11006 (2016).
29. Bruno, F. Y. *et al.* Observation of large topologically trivial Fermi arcs in the candidate type-II Weyl semimetal WTe₂. *Phys. Rev. B* **94**, 121112 (2016).
30. Wu, Y. *et al.* Observation of Fermi arcs in the type-II Weyl semimetal candidate WTe₂. *Phys. Rev. B* **94**, 121113 (2016).
31. Deng, K. *et al.* Experimental observation of topological Fermi arcs in type-II Weyl semimetal MoTe₂. *Nat. Phys.* **12**, 1105 (2016).
32. Fang, C., Chen, Y., Kee, H.-Y. & Fu, L. Topological nodal line semimetals with and without spin-orbital coupling. *Phys. Rev. B* **92**, 081201 (2015).
33. Neupane, M. *et al.* Observation of topological nodal fermion semimetal phase in ZrSiS. *Phys. Rev. B* **93**, 201104 (2016).
34. Hu, J. *et al.* Evidence of Topological Nodal-Line Fermions in ZrSiSe and ZrSiTe. *Phys. Rev. Lett.* **117**, 016602 (2016).
35. Schnyder, A. P., Ryu, S., Furusaki, A. & Ludwig, A. W. W. Classification of topological insulators and superconductors in three spatial dimensions. *Phys. Rev. B* **78**, 195125 (2008).
36. Fu, L. Topological crystalline insulators. *Phys. Rev. Lett.* **106**, 106802 (2011).
37. Slager, R.-J., Mesaros, A., Juricic, V. & Zaanen, J. The space group classification of topological band insulators. *Nat. Phys.* **9**, 98 (2013).
38. Jadaun, P., Xiao, D., Niu, Q. & Banerjee, S. K. Topological classification of crystalline insulators with space group symmetry. *Phys. Rev. B* **88**, 085110 (2013).
39. Shiozaki, K. & Sato, M. Topology of crystalline insulators and superconductors. *Phys. Rev. B* **90**, 165114 (2014).
40. Chiu, C.-K. & Schnyder, A. P. Classification of reflection-symmetry-protected topological semimetals and nodal superconductors. *Phys. Rev. B* **90**, 205136 (2014).
41. Sakintuna, B., Lamari-Darkrim, F. & Hirscher, M. Metal hydride materials for solid hydrogen storage: A review. *Int. J. Hydrogen Energy* **32**, 1121 (2007).
42. Smith, J. S., Desgreniers, S., Tse, J. S. & Klug, D. D. High-pressure phase transition observed in barium hydride. *J. Appl. Phys.* **102**, 043520 (2007).
43. Tse, J. S., Yao, Y. & Tanaka, K. Novel superconductivity in Metallic SnH₄ under High Pressure. *Phys. Rev. Lett.* **98**, 117004 (2007).
44. Jin, X. *et al.* Superconducting high-pressure phases of disilane. *Proc. Natl. Acad. Sci. USA* **107**, 9969 (2010).
45. Shamp, A. & Zurek, E. Superconducting high-pressure phases composed of hydrogen and iodine. *J. Phys. Chem. Lett.* **6**, 4067 (2015).

46. Duan, D. *et al.* Structure and superconductivity of hydrides at high pressures. *Natl. Sci. Rev.* **4**, 121 (2017).
47. Ashcroft, N. W. Metallic hydrogen: A high-temperature superconductor? *Phys. Rev. Lett.* **21**, 1748 (1968).
48. Ashcroft, N. W. Hydrogen dominant metallic alloys: High temperature superconductors? *Phys. Rev. Lett.* **92**, 187002 (2004).
49. Kim, D. Y., Scheicher, R. H. & Ahuja, R. Predicted High-Temperature Superconducting State in the Hydrogen-Dense Transition-Metal Hydride YH_3 at 40 K and 17.7 GPa. *Phys. Rev. Lett.* **103**, 077002 (2009).
50. Li, Y. *et al.* Pressure-stabilized superconductive yttrium hydrides. *Sci. Rep.* **5**, 9948 (2015).
51. Liu, H., Naumov, I. I., Hoffmann, R., Ashcroft, N. W. & Hemley, R. J. Potential high- T_c superconducting lanthanum and yttrium hydrides at high pressure. *Proc. Natl. Acad. Sci. USA* **114**, 6990 (2017).
52. Peng, F. *et al.* Hydrogen clathrate structures in rare earth hydrides at high pressures: Possible route to room-temperature superconductivity. *Phys. Rev. Lett.* **119**, 107001 (2017).
53. Liu, C.-C. *et al.* Low-energy effective hamiltonian for giant-gap quantum spin hall insulators in honeycomb x -hydride/halide ($x = \text{N}\sim\text{Bi}$) monolayers. *Phys. Rev. B* **90**, 085431 (2014).
54. Feng, W., Liu, C.-C., Liu, G.-B., Zhou, J.-J. & Yao, Y. First-principles investigations on the berry phase effect in spin-orbit coupling materials. *Comput. Mater. Sci.* **112**, 428 (2016).
55. Yang, B., Zhang, X. & Zhao, M. Dirac node lines in two-dimensional lieb lattices. *Nanoscale* **9**, 8740 (2017).
56. Yang, S. Y. *et al.* Symmetry demanded topological nodal-line materials. *arXiv:1707.04523v2* (2017).
57. Sjöstedt, E., Nordström, L. & Singh, D. J. An alternative way of linearizing the augmented plane-wave method. *Solid State Commun.* **114**, 15 (2000).
58. Madsen, G. K. H., Blaha, P., Schwarz, K., Sjöstedt, E. & Nordström, L. Efficient linearization of the augmented plane-wave method. *Phys. Rev. B* **64**, 195134 (2001).
59. Blaha, P., Schwarz, K., Madsen, G., Kvasnicka, D. & Luitz, J. *WIEN2k: An Augmented Plane Wave plus Local Orbitals Program for Calculating Crystal Properties* (Karlheinz Schwarz, Technische Universitaet Wien, Vienna, 2001).
60. Kuneš, J., Novák, P., Schmid, R., Blaha, P. & Schwarz, K. Electronic structure of fcc th: Spin-orbit calculation with $6p_{1/2}$ local orbital extension. *Phys. Rev. B* **64**, 153102 (2001).
61. Marzari, N. & Vanderbilt, D. Maximally localized generalized wannier functions for composite energy bands. *Phys. Rev. B* **56**, 12847 (1997).
62. Marzari, N., Mostofi, A. A., Yates, J. R., Souza, I. & Vanderbilt, D. Maximally localized wannier functions: Theory and applications. *Rev. Mod. Phys.* **84**, 1419 (2012).
63. Mostofi, A. A. *et al.* wannier90 : A tool for obtaining maximally-localised wannier functions. *Comput. Phys. Commun.* **178**, 685 (2008).
64. Sancho, M. P. L., Sancho, J. M. L. & Rubio, J. Quick iterative scheme for the calculation of transfer matrices: application to mo (100). *J. Phys. F:Met. Phys.* **14**, 1205 (1984).
65. Sancho, M. P. L., Sancho, J. M. L., Sancho, J. M. L. & Rubio, J. Highly convergent schemes for the calculation of bulk and surface green functions. *J. Phys. F:Met. Phys.* **15**, 851 (1985).
66. Udovic, T. J., Huang, Q. & Rush, J. J. Characterization of the structure of YD_3 by neutron powder diffraction. *J. Phys. Chem. Solids* **57**, 423 (1996).
67. Udovic, T. J., Huang, Q., Erwin, R. W., Hjärvansson, B. & Ward, R. C. C. Structural symmetry of YD_3 epitaxial thin films. *Phys. Rev. B* **61**, 12701 (2000).
68. Wang, Y. & Chou, M. Y. Peierls distortion in hexagonal YH_3 . *Phys. Rev. Lett.* **71**, 1226 (1993).
69. Pebler, A. & Wallace, W. E. Crystal structures of some lanthanide hydrides. *J. Phys. Chem.* **66**, 148 (1962).
70. Remhof, A. *et al.* Hydrogen and deuterium in epitaxial $\text{Y}(0001)$ films: Structural properties and isotope exchange. *Phys. Rev. B* **59**, 6689 (1999).
71. Fedotov, V. K., Antonov, V. E., Bashkin, I. O., Hansen, T. & Natkaniec, I. Displacive ordering in the hydrogen sublattice of yttrium trihydride. *J. Phys.: Condens. Matter* **18**, 1593 (2006).
72. Kelly, P. J., Dekker, J. P. & Stumpf, R. Theoretical prediction of the structure of insulating YH_3 . *Phys. Rev. Lett.* **78**, 1315 (1997).

73. Udovic, T. J., Huang, Q. & Rush, J. J. Comment on “Theoretical Prediction of the Structure of Insulating YH_3 ”. *Phys. Rev. Lett.* **79**, 2920 (1997).
74. Kelly, P. J., Dekker, J. P. & Stumpf, R. Kelly, Dekker, and Stumpf Reply:. *Phys. Rev. Lett.* **79**, 2921 (1997).
75. Udovic, T. J., Huang, Q. , Santoro, A. & Rush, J. J. The nature of deuterium arrangements in YD_3 and other rare-earth trideuterides. *Z. Kristallogr* **223**, 697 (2008).
76. Fu, L. & Kane, C. L. Topological insulators with inversion symmetry. *Phys. Rev. B* **76**, 045302 (2007).
77. Wu, Q., Zhang, S., Song, H.-F., Troyer, M. & Soluyanov, A. A. WannierTools: An open-source software package for novel topological materials. *arXiv preprint arXiv:1703.07789v1* (2017).

Acknowledgements

We thank the fruitful discussions with Jiawei Ruan, Huaiqiang Wang, Rui Wang, and Ying Xu. This work is supported by the MOST of China (Grant Nos: 2016YFA0300404, 2015CB921202), the National Natural Science Foundation of China (Grant Nos: 51372112 and 11574133), NSF Jiangsu province (No. BK20150012), the Fundamental Research Funds for the Central Universities, and Special Program for Applied Research on Super Computation of the NSFC-Guangdong Joint Fund (the second phase). Part of the calculations were performed on the supercomputer in the HPCC of Nanjing University and “Tianhe-2” at NSCC guangzhou.

Author contributions

J.S. supervised the project. D.S. and T.C. performed the calculations. D.S. and J.S. analysed the results and wrote the manuscript. All authors discussed the results, and commented on the manuscript.

Additional information

Competing financial interests: The authors declare no competing financial interests.